

Investigation of impurity driven corrosion behavior in molten 2LiF-BeF₂ salt

William H. Doniger^a, Cody Falconer^a, Mohamed Elbakhshwan^a, Karl Britsch^b, Adrien Couet^{a,b},
Kumar Sridharan^{a,b}

^a*University of Wisconsin-Madison Dept. of Materials Science & Engineering*

^b*Dept. of Engineering Physics, University of Wisconsin-Madison*

doniger@wisc.edu

Abstract

A 1000-hour corrosion experiment of 316H stainless steel at 700 °C investigated the role of metal fluoride impurities CrF₂ and FeF₂ in LiF-BeF₂ (66-34 mole %) (FLiBe) salt. Inductively coupled plasma-optical emission spectroscopy (ICP-OES) demonstrated the ability to measure changes in the concentration of these fluorides in FLiBe salt. Cyclic voltammetry (CV) showed the potential for real-time quantitative concentration measurement of corrosion products in the molten salt. Materials characterization revealed that both impurity species influence the dissolution of Cr from the alloy. The collective results from these analysis methods advance the understanding of the influence impurities have on materials corrosion.

Keywords Molten salt corrosion, 2LiF-BeF₂, 316H stainless steel, impurities, cyclic voltammetry

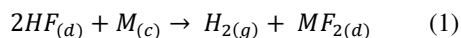
Introduction

The molten salt reactor (MSR) is a Generation IV reactor concept that offers improved safety, efficiency, and flexibility in fuel design. With the emergence of feasible solid-fueled molten salt reactor designs, such as the Fluoride-salt-cooled High-temperature Reactor (FHR), there is need for: (i) a greater understanding of materials' corrosion performance over long periods of exposure to non-fuel bearing LiF-BeF₂ (66-34 mole %) (FLiBe), the lead candidate for primary coolant in FHR, and (ii) the development of sensors to monitor and control corrosion in the molten FLiBe salt [1]. Historically, the Molten Salt Reactor Experiment (MSRE) at Oak Ridge National Laboratory (ORNL) utilized a liquid-fueled concept, wherein the uranium fuel was dissolved in a mixed fluoride salt solvent [2]-[3]. Here, chemical sensors relied on the measurements of redox behavior of the dissolved fuel to understand and control the corrosion of structural materials. While non-fuel bearing salts simplify the reactor coolant chemistry, new strategies for electrochemical sensors are required for non-fuel bearing FLiBe salt to monitor its corrosivity.

A potential sensor is made possible by probing the electrochemical nature of trace impurities from corrosion such as Fe and Cr in the FLiBe salt. Voltammetry methods sensitive to both dissolved CrF₂ and FeF₂ have previously been demonstrated in FLiBe salt at temperatures between 600 and 700 °C by some of the present authors [4]. In this research, the static, isothermal corrosion experiments have been performed to evaluate the effect of CrF₂ and FeF₂ impurities on corrosion of 316H stainless steel (referred to henceforth as 316H) in conjunction with electrochemistry experiments to monitor changes in the impurity concentrations. Such a study could form the basis for the development of new on-line electrochemical sensors to monitor the corrosion of materials.

The need for improved methods to characterize the rate at which materials corrode in molten salts motivates electrochemical sensor development. Given the instability of the protective passivating oxide layer in molten fluoride salt environments, the corrosion rate depends on the thermodynamic driving force for the dissolution of alloying elements into the salt and the rate of diffusion of alloying elements from the bulk towards the material surface [5]. The introduction of impurities such as moisture, oxygen, and metals into the salt affects corrosion if they react favorably with some alloying elements. The ingress of these impurities is possible even when best efforts are made to maintain stable salt environments.

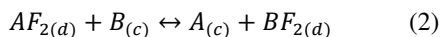
Impurities in the salt provide pathways for corrosion by forming relatively unstable fluorides, such as HF, with the tendency to corrode vessel materials by a reaction such as,



where the symbols (d), (c) and (g) denote dissolved, crystalline and gaseous species, respectively. Empirically, the most common corrosion product of structural alloys in molten FLiBe salt is dissolved Cr^{2+} . Its susceptibility is correlated to its relatively negative Gibb's free energy of formation [3], [6].

The intrinsic standard electrode potentials of some redox couples dissolved in FLiBe with respect to the theoretical $HF(g)/H_2(g)$ reference reaction have been measured enabling more direct comparison [6-7]. Of the major elements constituting structural alloys (Cr, Fe, and Ni), Cr/ Cr^{2+} couple has the most negative standard electrode potential and therefore oxidation of Cr is most energetically favorable when comparing solutions of each of these dilute impurities under a standard set of conditions.

Redox reactions between dilute metal fluorides provide additional mechanisms for corrosion. Manly et al. [8] showed that the activity of Fe and Ni dissolved in NaF_4 - ZrF_4 - UF_4 (50-46-4 mole %) had a dramatic effect on the degree of void formation in Inconel alloy thermal-convection-loops after 500 hours at 815 °C. The general equilibrium of the reaction of the metal impurity fluoride AF_2 dissolved in the salt and the metal alloying element B,



is governed by the relative chemical stability of fluorides composed of A and B. Here the free energy of formation of the BF_2 is more negative than AF_2 resulting in preferential corrosion of the alloying element B. For example, a salt with high FeF_2 activity in the salt may leave components with Cr alloying additions vulnerable to dissolution in the salt.

The rate at which corrosion occurs also depends on the pathway for alloying elements to migrate to the materials' surface. One study has shown that the primary path for Cr diffusion depends on temperature [9]. For example, in Inconel alloy, above 800 °C, the diffusion of Cr and vacancies is relatively high and depleted elements are replaced by vacancies that coalesce and form voids. Corrosion below 800 °C was typically characterized by a selective attack of chromium and was accelerated along high diffusion rate pathways, such as grain boundaries, suggesting that temperature influences elemental distribution induced by corrosion. This research targets corrosion tests at 700 °C as a temperature more relevant to the FHR and studies the influence of corrosion products on the depletion of Cr in a regime where grain boundary diffusion likely dominates. The material investigated is 316H, which is presently the lead candidate structural material for FHR.

A survey of much of the relevant corrosion data in molten halide salts available in the literature [10] reveals unresolved inconsistencies stemming from factors such as variations in salt purity, experimental design, salt type (fluoride vs. chloride), and the test material. To address these inconsistencies, the present study uses a combination of static corrosion tests with associated materials characterization, analytical chemistry, and electrochemistry to elucidate the understanding of corrosion of 316H in molten FLiBe salt. The FLiBe used in this study was purified by the hydrofluorination process and pre-determined trace quantities of CrF_2 and FeF_2 impurities were intentionally dissolved in this salt to understand their role in materials corrosion. The results of the study could potentially serve as a basis for the deployment of electrochemical sensors in future molten salt corrosion experiments and in the FHR where 316H is being considered structural material.

Experimental Methods

The electrochemical behavior of dissolved corrosion products has been investigated to correlate salt chemistry with corrosion-induced compositional changes in the near-surface regions of 316H. Samples of 316H were exposed to four FLiBe salt chemistries for 1000 hours at 700°C. To simulate the dissolved corrosion products in FLiBe, pre-measured quantities of divalent chromium and iron fluorides were added

to the salt. Electrochemical and corrosion experiments were conducted in an inert argon atmosphere glove box. Oxygen and moisture levels were maintained below 1 ppm and 2 ppm, respectively.

Each salt was prepared from high-purity FLiBe salt produced at the University of Wisconsin – Madison [11]. Lithium-fluoride (99.8% purity) was obtained from Noah Technologies and beryllium-fluoride (98.8% purity) was purchased from Materion. The 40 kg batch was hydrofluorinated, a process that involves sparging of the salt melt with both hydrogen and hydrogen-fluoride to remove trace impurities such as oxygen and moisture. FeF₂ with 99.9% purity obtained from Apollo Scientific and CrF₂ of 99% purity obtained from Synquest Laboratories were added in pre-measured quantities to this FLiBe salt to simulate the corrosion products in the molten salt.

Electrochemical experiments were conducted in a glassy carbon crucible at 700°C using a scan rate of 80 mV/sec. The electrochemical cell featured a glassy carbon counter electrode (CE), molybdenum working electrode (WE) and a molybdenum quasi-reference electrode (QRE). Molybdenum electrodes were polished to 1200 grit. The WE surface area was calculated using the diameter (2 mm) and the insertion depth in the salt. WE surface areas ranged between 0.8 and 1.2 cm². Voltammetry was conducted with a Metrohm Autolab 128N potentiostat. The development of these electroanalytical techniques has been described in our previous paper [4]. Results are reported with respect to the Be/BeF₂ redox couple. The reference potential is acquired for each CV using a dynamic beryllium reference electrode (DBRE).

316H was selected for this investigation because it is ASME Section III Division 5 code certifiable for mechanical properties at 700°C and is the lead candidate structural material for the FHR. Each static isothermal corrosion cell consisted of three 316H coupons contained in a 316L stainless steel capsule. The carbon content of 316H is the only significant compositional difference between the two materials as shown in Table 1, eliminating the possibility of dissimilar materials corrosion. The corrosion capsules are made from 86.36 mm diameter 316L stainless steel tube with 1.651 mm thick walls. A steel bottom cap was welded onto the tube end using a 316 stainless steel filler rod. The top was loosely fitted with a steel lid. Three corrosion coupons were suspended from the lid by 316 stainless steel wire. The 316H stainless steel sample coupons were cut using wire EDM from plate and were 16.5 mm x 12.1 mm x 1.5 mm with two 1.7 mm diameter holes drilled in each end to suspend the coupons. The surface area of a coupon was 4.9 cm².

Each capsule contained 35 g of FLiBe salt. Using the mass and the density of pure FLiBe reported by Williams [12] of $2.280 - 0.00488 \cdot T[^\circ\text{C}]$ g/cm³ the calculated salt volume of each capsule was determined to be 17.4 ml. The total surface area of the 316H coupon and 316 stainless steel capsule exposed to the liquid salt were 14.5 cm² and 48.4 cm², respectively. The ratio of the total stainless steel surface area to salt volume was 3.62 cm⁻¹.

Table 1. Nominal compositions of 316H and 316L and the certified composition of the as-received austenitic stainless steel used in this study in weight percent [13].

Alloy	Spec.	Cr	Ni	Mo	C	Mn	P	S	Si	N	Fe
316H UNS S31609	Min	16	10	2	0.04						
	Max	18	14	3	0.1	2	0.045	0.03	0.75	0.1	Balance
316L UNS S31603	Min	16	10	2							
	Max	18	14	3	0.03	2	0.045	0.03	0.75	0.1	Balance
As-received 316H		16.07	10.08	2.09	0.05	0.84	0.027	0	0.5	0.04	Balance

To determine the composition of the salt before and after corrosion as well as to benchmark electrochemical experiments, the analysis of the metal impurity content in FLiBe salt was performed at the Wisconsin State Laboratory of Hygiene using inductively coupled plasma – optical emission spectroscopy (ICP-OES).

Scanning electron microscopy (SEM) coupled with X-ray dispersive spectroscopy (EDS) and X-ray diffraction (XRD) were performed at the Wisconsin Center for Nanoscale Technology to characterize the pre- and post-corrosion samples. Before analysis, the salt was removed from samples using ultrasonic cleaning in deionized water, acetone, and alcohol. Cross-sectional microscopy of the samples was performed by first coating the sample surface with copper before mounting in Bakelite to protect the integrity of the exposed surface of the samples during metallographic sample preparation.

Results

ICP-OES

The cationic concentrations of the salt were measured using ICP-OES before and after the corrosion experiments as a measure of the magnitude of corrosion of 316H. Table 2 shows the concentration of the predominant trace metal impurities (Cr, Fe, Mn, Ni) in each capsule salt before and after exposure. Capsule 1 contained as-purified FLiBe salt that initially had less than 15 ppm of Cr, Mn, and Ni. The initial salt composition of capsule 2, where CrF_2 was added, contained 245 ± 3 ppm Cr. Capsules 3 and 4, where FeF_2 was added, contained 99 ppm and 392 ppm Fe, respectively. The limit of quantification (LOQ) for Fe is approximately 65 ppm.

After exposure, the Cr content in the salt increased for all capsules, as expected based on Reactions 1 and 2. The concentration of the predominant dilute metals after exposure are shown in Table 2. In addition to Cr, the depletion of manganese is an important corrosion phenomenon for some steels in molten salts [14]. Mn is a minor alloying element in stainless steel. Salts in all capsules experienced an increase in Mn concentration of approximately 40 to 50 ppm. The free energy of the formation of MnF_2 in molten FLiBe is even more negative than CrF_2 , meaning that the formation of MnF_2 as a corrosion product is highly favorable energetically [15].

The changes in Fe concentration of capsules 3 and 4 result from impurity driven corrosion. The concentration of Fe in these salts dropped below the LOQ as a result of exposure to 316 stainless steel. The corresponding increase in Cr content after corrosion is believed to occur by reaction 2. The largest net change in concentration of chromium occurred in capsule 4 with a higher initial concentration of FeF_2 .

Table 2. ICP-OES metals analysis before and after corrosion tests. The limit of quantification (LOQ) for Fe is approximately 65 ppm. Values below the LOQ are not reported.

Capsule	Before-corrosion				After-corrosion			
	Cr	Fe	Mn	Ni	Cr	Fe	Mn	Ni
	(ppm)				(ppm)			
1	6 ± 1	-	4.2 ± 0.4	14 ± 3	263 ± 7	-	40 ± 1	8.5 ± 0.3
2	245 ± 3	-	3.8 ± 0.4	14 ± 3	452 ± 3	-	47.2 ± 0.2	8.7 ± 0.1
3	7 ± 1	99	3.4 ± 0.4	11 ± 3	219 ± 5	-	42.4 ± 0.8	9.6 ± 0.1
4	6 ± 1	392	3.5 ± 0.4	10 ± 3	450 ± 8	-	55.7 ± 0.2	9.3 ± 0.1

Voltammetry

As mentioned above, cyclic voltammetry (CV) techniques are a useful supplement to ICP methods for understanding corrosion with potential for use for in situ analysis of molten salts. Figure 1 shows the CVs of salts in capsules 1 through 4 before and after exposure to 316H for 1000 hours at 700 °C. Anodic (positive) and cathodic (negative) current peaks correspond to oxidation and reduction of electroactive species, respectively. The magnitude and potential at which the current peaks occur are dependent upon the identity of the species and its activity in the melt.

In each CV, it is assumed that the pair of anodic and cathodic peaks with the lowest potential with respect to Be/BeF_2 reference reaction corresponds to the general half-cell reaction,

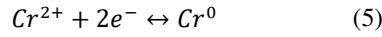


where soluble M^{n+} is in equilibrium with insoluble M . If electrolysis fully covers the surface of the electrode with M , the activity of the deposit is unity and reaction 3 will have a half-cell reduction potential given by the Nernst's equation,

$$E_{(M^{n+}/M)} = E_{(M^{n+}/M)}^{\circ} - \frac{RT}{nF} \ln\left(\frac{1}{a_{M^{n+}}}\right) \quad (4)$$

where R is the gas constant, T is the temperature, and F is Faraday's constant. In this experiment, a half-cell reduction potential is determined by the number of electrons, n , the activity of M^{n+} , $a_{M^{n+}}$, and $E_{(M^{n+}/M)}^{\circ}$, which is the standard potential of the M^{n+}/M couple in the molten salt mixture with respect to an arbitrary thermodynamic reference point. In our previous work [4], it was shown that the Cr/Cr^{2+} redox couple is a reversible reaction at 700 °C with a half-cell reduction potential that obeys equation 4. A method that uses the variation in CV peak potentials as a metric for changes in reduction potential was developed in [4] and is adopted here. Comparisons of the anodic and cathodic peak potentials, $E_{p,a}$ and $E_{p,c}$, are made to identify the species M participating in reaction 3.

The most obvious change occurred in capsule 1, which contained as-purified FLiBe salt. In Figure 1 (a), the CV of the as-purified FLiBe before corrosion (dotted line) has no significant redox peaks indicating that the concentrations of dissolved species, such as Cr^{2+} and Fe^{2+} , are low. ICP-OES reveals that after corrosion the Cr concentration of capsule 1 increased from 6 ± 1 ppm to 263 ± 7 ppm. In the CV after corrosion (solid line), the redox peaks 5a and 5c have peak potentials at 1.10 and 0.95 V vs. Be/BeF_2 , respectively. Comparison of the peak potentials to previous work indicates that the reaction corresponds to the Cr/Cr^{2+} redox couple,

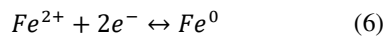


which is generally observed between 0.8 V and 1.2 V vs. Be/Be^{2+} at 700 °C [4].

The CVs of the salt in capsule 2 show the sensitivity of the technique to changes in the analyte concentration that is approximately consistent with the results of ICP-OES metals analysis. As shown in Table 2, the Cr in capsule 2 increased from 245 ± 3 ppm to 452 ± 3 ppm after exposure to 316H. In Figure 1 (b), CVs before and after corrosion show an increase in the activity of a dissolved species. The cathodic peak potential of reaction 5 increases by approximately 40 mV. This is only slightly higher than the 26 mV change in $E_{(\text{Cr}^{2+}/\text{Cr})}$ calculated by using the concentration of Cr in capsule 2 before and after corrosion in equation 4 and taking the difference. While this method of determining concentration is not accurate, since $a_{M^{n+}}$ is unknown and its relation to potential is logarithmic, it is clear that corrosion has led to a measurable change in salt chemistry that is observed at least qualitatively by CV.

The exact cause of the apparent corrosion in capsules 1 and 2 remains somewhat speculative. There are two plausible causes. First, the purification of fluoride salts is an imperfect process. Trace impurities that may not be accounted for in the available data may contribute to corrosion. A comparison of purified vs. non-purified salt was not performed in this study. Second, while the atmosphere was maintained to a high standard compared to industrial and research standards, it is theoretically still possible for a small amount of impurities to get incorporated into the salt and produce HF enabling reaction 1 to proceed. A method of sampling the FLiBe salt's HF concentration that would not potentially be detrimental to the corrosion experiment was not available.

A remarkable change in salt chemistry is observed with CVs in capsules 3 and 4. Initial salt mixtures containing 99 ppm Fe and 392 ppm Fe showed redox peaks 6a and 6c between 1.2 and 1.5 V vs. Be/Be^{2+} at 700 °C which corresponds to the reaction,



Following corrosion, new anodic and cathodic peaks lie between 0.8 V and 1.2 V vs. Be/Be²⁺ at 700 °C. The change in the reduction potentials of the dominant redox peaks is quite large. According to equation 4, a large decrease in Fe²⁺ concentration could lead to a change in $E_{(Fe^{2+}/Fe)}$ of several hundred mV, but the intensity of the current density peaks would become much smaller than peak 6c. It is therefore likely that peaks 5a and 5c correspond to a species with a lower standard reduction potential. The decrease in Fe and increase in Cr concentrations in capsules 3 and 4, shown in Table 2, after corrosion leads to the conclusion that peaks 5a and 5c correspond to the Cr/Cr²⁺ redox couple.

While the dominant set of redox peaks observed in each CV are consistent with the expected dissolved species, distortions of some of the redox peaks suggest that more complex electrochemical phenomena are present, as observed in several scans including for capsule 2 before corrosion and all capsules post corrosion. Possible origins for these peaks have been previously discussed, including underpotential deposition, and other possible soluble-soluble reactions [4]. These immutable peaks are indicative of additional redox reactions whose redox behavior is convoluted with that of the redox reaction of interest.

The redox couple(s) which appear in addition to the Cr/Cr²⁺ redox reaction after corrosion are speculated to have several possible identities. For instance, dissolved chromium fluoride may likely take on II and III oxidation states in FLiBe [16]. Other salt contaminants may raise or lower the activity of Cr²⁺ and Cr³⁺. Dissolved manganese is also electrochemically active and can produce current peaks of its own. The reduction potential of a soluble-insoluble redox reaction of Mn relative to that of Cr/Cr²⁺ will depend on their relative activities. The concentration of Mn measured by ICP-OES is significant enough that an appreciable electrochemical reaction could conceivably be measured with CV. Neither the effect of dissolved FeF₂ on the ratio of the Cr²⁺/Cr³⁺ activities nor the electrochemical behavior of the Mn redox couple have been extensively studied in FLiBe.

While the ability to reliably distinguish some corrosion products, such as Cr²⁺ and Fe²⁺, from one another is beneficial to salt chemistry and corrosion research, the occurrence of more than one set of redox peaks in close proximity presents a challenge for quantitative CV analysis. A quantitative approach to analysis taken in previous work [4] and other experiments [17]-[21] assumes that the electrochemical system consists of a redox couple between a single soluble reactant and an insoluble product, such as reaction 4. The model does not explicitly deal with the case in which more than one electrochemically active, soluble species is present. Several studies [22]-[23] have discussed the implementation of more rigorous theoretical approaches to quantitative CV analysis.

Weight change analysis

The weight change of 316H was measured after exposure to each salt chemistry to quantify the effect of the imposed conditions. In Figure 2, the average weight change of three 316H coupons placed in capsules 1 through 4 is shown. All samples experience mass loss. While significant changes in salt chemistry were observed in each capsule, it is difficult to interpret the effect of each salt chemistry based on weight change alone.

The as-purified salt in capsule 1 provides a benchmark to compare other samples in this study. These samples experienced an average weight loss of 0.26 ± 0.05 mg/cm². This is comparable to results from experiments that exposed 316L stainless steel to similar salts and the same capsule material. Zheng et al. [24] found that 316L stainless steel experienced approximately 0.2 mg/cm² of weight loss when exposed to as-purified ⁷Li enriched MSRE FLiBe salt for 1000 hours at 700 °C. Chrobak [25] reported that 316L stainless steel exposed to as-purified non-⁷Li enriched FLiBe salt for 2000 hours at 700 °C showed 0.90 ± 0.05 mg/cm² of weight loss.

When compared to capsule 1, the weight change results of coupons in the other capsules are not statistically very different. As shown in Figure 2, the coupons in capsule 2 experienced the lowest average weight loss of 0.198 ± 0.004 mg/cm². Capsules 3 and 4 showed 0.22 ± 0.07 mg/cm² and 0.24 ± 0.04

mg/cm² of weight loss, respectively. Given the uncertainty, the weight change results suggest that all capsules experience the same net corrosion. To better assess materials degradation, microstructural characterization was performed using X-ray Diffraction (XRD), scanning electron microscopy (SEM), energy dispersive spectroscopy (EDS).

Post corrosion material characterization analysis

XRD performed on 316H following corrosion showed some microstructural modification of the surface. Figure 3 shows that varying amounts of austenite and ferrite are present on the surface of 316H exposed to the different salt chemistries. Austenite (111), (110), and (220) peaks are present in all samples. The ferrite (110) peak is observed in the as-received 316H while the additional ferrite (110), (200) and (211) peaks are observed in coupons exposed to as-purified FLiBe and FLiBe containing FeF₂. Zheng et al. [24] showed that 316L stainless steel exposed to as-purified ⁷Li enriched FLiBe resulted in ferrite phase formation in the near-surface region of the sample. Investigation of the ferrite content as a function of depth revealed little ferrite in the bulk suggesting that the phenomenon is not thermally induced, but rather corrosion-induced. There is variation in the intensity of the austenite (111) and ferrite (110) peaks. A comparison of these two peaks shows the significant formation of ferrite in as-purified FLiBe and FLiBe with FeF₂. There is little correlation between impurity activity and ferrite formation. Interestingly, no ferrite formation is observed in (c), the samples from the capsule which contained FLiBe with CrF₂. The exact mechanism for ferrite formation when steel is exposed to FLiBe remains unclear, as the loss of Cr should stabilize austenite rather than ferrite. It is also possible that the peaks identified as ferrite could be caused by other phases, such as the Mo-rich precipitates.

The near-surface regions of coupons in capsules 1 through 4 were examined using SEM for the influence of each salt chemistry. The exposed surface of each 316H coupon is shown in Figure 4. Different salt mixtures resulted in different amounts of surface roughening. Small particles with diameters less than 1 micrometer were prevalent on samples exposed in capsule 1 and some were observed on samples in capsules 2 and 3. EDS analysis confirmed the observation, first made by Zheng [24], that the particulates observed on the surface of steel after exposure to as-purified FLiBe are molybdenum-rich. The exact origin of the particles is not exactly known. The depletion of Cr may promote the precipitation of Mo in the near-surface region. If this hypothesis is true, the higher density of Mo-rich precipitates in Figure 4 (a) than in Figure 4 (b) may indicate that the coupons in capsule 1 experienced more Cr depletion than in capsule 2. Further characterization was performed on samples in capsules 3 and 4 to better understand why no Mo precipitates appear on their surfaces.

A coupon from each capsule was cross-sectioned and analyzed using EDS to determine how each salt chemistry affects the distribution of alloying elements in the near-surface region. In Figure 5, EDS compositional line scans through a grain in the near-surface region of each coupon show the elemental depletion from the bulk of 316H grains. No significant depletion of Cr from the 316H bulk grain was observed at this temperature. In capsules 1 and 2, the concentration of Cr in the bulk grain at the surface decreases only by a few weight percent. This implies that, at this temperature, corrosion at the exposed grain surface occurs very slowly and supports the hypothesis that the majority of Cr depletion occurs at the grain boundary where Cr can diffuse towards the surface at a higher rate.

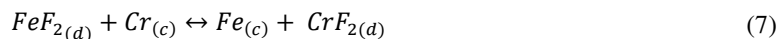
The morphology and compositional of the near surface region of coupons in each capsule were analyzed using SEM and EDS compositional maps. Figure 6 (a), (d), (g), (j) show SEM images of coupons in capsules 1-4. Figure 6 (b), (e), (h), (k) show EDS compositional maps of chromium in each coupon. Figure 6 (c), (i), (l), (m) show EDS compositional maps of iron in each coupon. In each SEM image a grain boundary that intersects the exposed surface is visible. In all capsules, EDS analysis shows that the grain boundaries in the bulk material, away from the exposed surface, are deficient in Fe and rich in Cr. The Cr rich precipitates are likely chromium carbides resulting from extensive thermal aging at these high corrosion test temperatures. In the near-surface region, there are, however, distinct differences in the distribution of Cr and Fe as a result of exposure to each salt chemistry. To account for the different

surface features the *depth of corrosion attack* was measured in terms of chromium depletion depth along grain boundaries rather than with respect to the apparent exposed surface. Figure 6 (b) shows that there is a depletion of Cr from the grain boundary to a length of 7.7 μm in capsule 1, while it is difficult to determine an appreciable depth of corrosion attack in capsule 2, as shown Figure 6 (e). Figure 6 (h) and Figure 6 (k) show coupons from capsules 3 and 4 which suffered corrosion attack to a depth of 3.1 μm and 8.8 μm . Additionally, these coupons also show an unusual Cr deficient and Fe rich layer parallel to the exposed surface.

In Figure 6 (b), the 7.7 μm depth of corrosion attack in as-purified FLiBe is consistent with similar experiments in purified FLiBe which showed depths of corrosion attack on the order of 5 to 10 μm in 1000 hours at 700 $^{\circ}\text{C}$ [24]. Interestingly, the different material grain size and surface density of grain boundaries found in [24] do not dramatically change the depth of corrosion attack. This supports the hypothesis that, at this temperature, transport of Cr to the material surface is largely governed by the rate of diffusion of Cr along grain boundaries.

The addition of CrF_2 decreased the apparent grain boundary attack depth, as shown in Figure 6. The near-surface region also experienced less Cr depletion, consistent with the weight loss data in Figure 3. The increase in Cr concentration in the salt in capsule 2 after corrosion, shown by both ICP-OES and electrochemistry, signifies that 316H is still susceptible to some corrosion of Cr even in the presence of relatively high activity chromium fluoride.

In capsules 3 and 4, unlike capsules 1 and 2, 316H exposed to salts with high levels of dissolved FeF_2 show a unique surface feature that is not typically present after exposure to purified FLiBe. In Figure 6 (i) and (l), there is an emergence of a Fe rich surface layer that could be linked to the low net weight change of the exposed material. Two possible explanations for the emergence of the Fe rich layer have been considered. The first is that corrosion enhanced by the high activity of Fe^{2+} may lead to more aggressive corrosion not only at the grain boundaries but also in the bulk material. This may partially explain the occurrence of the Cr deficient layer but does not adequately account for the disappearance of Fe originally dissolved in the salt. The second explanation is a reaction involving the simultaneous oxidation of Cr and reduction of Fe metal at the exposed surface.



Comparing capsules 1 and 4, both ICP-OES and electrochemical methods indicated that FLiBe which initially contained 392 ppm FeF_2 contained almost twice the amount of Cr present in as-purified FLiBe post corrosion, yet the weight change of 316H stainless steel coupons in these capsules are comparable in Figure 2. The simultaneous dissolution of Cr and deposition of reduced iron decrease the net weight loss of the material. Reaction 7 explains both the microstructural features present in Figure 6 (i) and (l) and the small net change in the weight of the coupons.

EDS compositional line scans were used to further investigate the nature of the surface layer on coupons in capsules 3 and 4. Figure 5 (c) and (d) show an obvious deficiency in Cr at the material surface, but there is still appreciable Cr in the first 3 μm of material thickness. The Cr concentration profile extended 5 μm into the material suggesting that Cr from the alloy bulk diffuses into the Fe rich surface layer.

ICP-OES, electrochemistry and materials characterization determined that the rate of corrosion in salt-containing 99 ppm FeF_2 is lower than as-purified FLiBe, a surprising conclusion given that raising the activity of FeF_2 was hypothesized to lead to increased corrosion. One plausible explanation, based on EDS analysis, is that the deposition of Fe on the sample surface forms a diffusion barrier. Cr from the bulk material would be required to diffuse through the developing iron-rich layer to sustain reaction 6 as the dominant corrosion mechanism in capsules 3 and 4. The non-zero concentration of Cr at the material surface shows that the rate of diffusion is sufficient to allow reaction 7 to proceed. It is, therefore, possible that most dissolved FeF_2 can participate in reaction 7. This is consistent with ICP-OES and

electrochemistry results that show that the salt has decreased to levels of FeF_2 below the LOQ following exposure to 316H. The results of capsules 3 and 4 show a strong correlation between the concentration of Fe^{2+} and Cr^{2+} before and after corrosion that is consistent with the hypothesized impurity driven corrosion.

Conclusions

Analytical chemistry, electrochemistry, and materials characterization before and after corrosion tests are essential tools in understanding the influence of CrF_2 and FeF_2 impurities in the salt on corrosion of 316H stainless steel in molten FLiBe salt. Both inductively coupled plasma-optical emission spectroscopy and cyclic voltammetry methods show promise for measurement of trace impurities and confirm that chromium is the predominant corrosion product of 316H stainless steel. In all cases, 316H stainless steel experienced mass loss, however, the mass loss measurements alone did not yield a discernible difference despite the clear differences in salt chromium content after corrosion. Additional, SEM, EDS compositional analysis, and XRD showed the unique influence that each impurity had on the surface of 316H stainless steel and provide additional insight into the weight change results. Voltammetry techniques applied for the determination of dilute species concentration demonstrate the ability to distinguish between common corrosion products, such as dissolved CrF_2 and FeF_2 . Further development of voltammetry methods is required to understand the shape of the CV waveform after corrosion. Dissolved CrF_2 and FeF_2 have several effects on the microstructure and weight change of 316H. Residual impurities in FLiBe following purification by hydrofluorination can lead to an appreciable depletion of Cr along grain boundaries and mass loss. Corrosion is somewhat decreased but not eliminated by the higher activity of CrF_2 in the salt. The depletion of Cr and the development of a Fe-rich surface layer in salts that initially contained FeF_2 demonstrate the importance of impurity driven corrosion.

Acknowledgments

This work was supported by the U.S. Department of Energy Integrated Research Project Nuclear Energy University Program under contract No. DE-NE0008285. The authors gratefully acknowledge the use of facilities and instrumentation at the UW-Madison Wisconsin Centers for Nanoscale Technology (wcnt.wisc.edu) partially supported by the NSF through the University of Wisconsin Materials Research Science and Engineering Center (DMR-1720415). The authors would like to acknowledge the assistance of Wisconsin State Laboratory of Hygiene for performing inductively coupled plasma-optical emission spectroscopy (ICP-OES) analysis of the salt samples.

Data Availability

The raw/processed data required to reproduce these findings cannot be shared at this time as the data also forms part of an ongoing study.

References

- [1] C. W. Forsberg, P. F. Peterson, K. Sridharan, L. Hu, M. Fratoni, and A. K. Prinja, "Integrated FHR technology development: Tritium management, materials testing, salt chemistry control, thermal hydraulics and neutronics, associated benchmarking and commercial basis," Massachusetts Inst. of Technology (MIT), Cambridge, MA (United States). Center for Advanced Nuclear Energy Systems (CANES); Univ. of California, Berkeley, CA (United States); Univ. of Wisconsin, Madison, WI (United States); Univ. of New Mexico, Albuquerque, NM (United States), DOE-MIT-0008285, Oct. 2018.
- [2] F. R. Clayton, G. Mamantov, and D. L. Manning, "Electrochemical Studies of Uranium and Thorium in Molten $\text{LiF} - \text{NaF} - \text{KF}$ at 500°C ," *J. Electrochem. Soc.*, vol. 121, no. 1, pp. 86–90, Jan. 1974, doi: 10.1149/1.2396838.
- [3] R. E. Thoma, "Chemical Aspects of MSRE Operations - ORNL - 4658." Oak Ridge National Lab, Tenn, 1971.

- [4] W. H. Doniger and K. Sridharan, "Application of voltammetry for quantitative analysis of chromium in molten 2LiF-BeF₂ (FLiBe) salt," *J. Electroanal. Chem.*, vol. 838, pp. 73–81, Apr. 2019, doi: 10.1016/j.jelechem.2019.02.048.
- [5] J. H. DeVan and R. B. Evans III, "Corrosion Behavior of Reactor Materials In Fluoride Salt Mixtures," Oak Ridge National Laboratory, Metals and Ceramics Division, ORNL-328, Sep. 1962.
- [6] W. R. Grimes, "Molten-Salt Reactor Chemistry," *Nucl. Appl. Technol.*, vol. 8, pp. 137–155, Feb. 1970.
- [7] C. F. J. Baes, "The chemistry and thermodynamics of molten salt reactor fuels," *Nucl Met Met Soc AIME 15 617-44*, 1969.
- [8] W. D. Manly, G. M. Adamson, J. H. Coobs, J. H. DeVan, and D. A. Douglas, "Aircraft Reactor Experiment-Metallurgical Aspects," Oak Ridge National Laboratory, Oak Ridge National Laboratory, Oak Ridge, Tennessee, AEC Research and Development Report ORNL-2349, Dec. 1957.
- [9] R. B. Evans, *Self-diffusion of chromium in nickel-base alloys*. Oak Ridge National Laboratory, 1961.
- [10] S. S. Raiman and S. Lee, "Aggregation and data analysis of corrosion studies in molten chloride and fluoride salts," *J. Nucl. Mater.*, vol. 511, pp. 523–535, Dec. 2018, doi: 10.1016/j.jnucmat.2018.07.036.
- [11] B. C. Kelleher, K. P. Dolan, P. Brooks, M. H. Anderson, and K. Sridharan, "Batch-Scale Hydrofluorination of Li₂BeF₄ to Support Molten Salt Reactor Development," *J. Nucl. Eng. Radiat. Sci.*, vol. 1, no. 4, pp. 041010/1-041010/12, 2015, doi: 10.1115/1.4030963.
- [12] D. F. Williams, L. M. Toth, and K. T. Clarno, "Assessment of Candidate Molten Salt Coolants for the Advanced High-Temperature Reactor," Oak Ridge National Laboratory, Nuclear Science and Technology Division, ORNL/TM-2006/12, Mar. 2006.
- [13] "Alloy 316H Stainless Steel Plate," *Sandmeyer Steel*. [Online]. Available: <https://www.sandmeyersteel.com/316-316L.html>. [Accessed: 25-Oct-2019].
- [14] M. Elbakhshwan *et al.*, "Corrosion and Thermal Stability of CrMnFeNi High Entropy Alloy in Molten FLiBe Salt," *Sci. Rep.*, vol. 9, no. 1, Dec. 2019, doi: 10.1038/s41598-019-55653-2.
- [15] J. Zhang *et al.*, "Redox potential control in molten salt systems for corrosion mitigation," *Corros. Sci.*, vol. 144, pp. 44–53, Nov. 2018, doi: 10.1016/j.corsci.2018.08.035.
- [16] H. G. MacPherson, "Molten-Salt Reactor Program Quarterly Progress Report: October 1958," ORNL 2626.
- [17] P. Delahay, *New instrumental methods in electrochemistry; theory, instrumentation, and applications to analytical and physical chemistry. With a chapter on high-frequency methods*. New York: Interscience Publishers, 1954.
- [18] T. Berzins and P. Delahay, "Oscillographic Polarographic Waves for the Reversible Deposition of Metals on Solid Electrodes," *J. Am. Chem. Soc.*, vol. 75, no. 3, pp. 555–559, Feb. 1953, doi: 10.1021/ja01099a013.
- [19] M. M. Tylka, J. L. Willit, J. Prakash, and M. A. Williamson, "Method development for quantitative analysis of actinides in molten salts," *J. Electrochem. Soc.*, vol. 162, no. 9, pp. H625–H633, 2015, doi: 10.1149/2.0401509jes.
- [20] A. Lugovskoy, M. Zinigrad, and D. Aurbach, "Electrochemical Determination of Diffusion Coefficients of Iron (II) Ions in Chloride Melts at 700–750°C," *Isr. J. Chem.*, vol. 47, no. 3–4, pp. 409–414, Dec. 2007, doi: 10.1560/IJC.47.3-4.409.
- [21] D. Shen and R. Akolkar, "Electrodeposition of Neodymium from NdCl₃-Containing Eutectic LiCl–KCl Melts Investigated Using Voltammetry and Diffusion-Reaction Modeling," *J. Electrochem. Soc.*, vol. 164, no. 8, pp. H5292–H5298, 2017, doi: 10.1149/2.0451708jes.
- [22] A. M. Keightley, J. C. Myland, K. B. Oldham, and P. G. Symons, "Reversible cyclic voltammetry in the presence of product," *J. Electroanal. Chem.*, vol. 322, no. 1, pp. 25–54, Jan. 1992, doi: 10.1016/0022-0728(92)80065-C.
- [23] S. Guo, N. Shay, Y. Wang, W. Zhou, and J. Zhang, "Measurement of europium (III)/europium (II) couple in fluoride molten salt for redox control in a molten salt reactor concept," *J. Nucl. Mater.*, vol. 496, pp. 197–206, Dec. 2017, doi: 10.1016/j.jnucmat.2017.09.027.

- [24] G. Zheng, B. Kelleher, G. Cao, M. Anderson, T. Allen, and K. Sridharan, "Corrosion of 316 Stainless Steel in High Temperature Molten Li_2BeF_4 (FLiBe) Salt," *J. Nucl. Mater.*, vol. 461, pp. 143–150, Mar. 2015.
- [25] T. Chrobak, "Corrosion of Candidate Materials in Molten FLiBe Salt for Application in Fluoride-salt Cooled Reactors," Thesis, University of Wisconsin - Madison, Madison, WI, 2018.

Figures

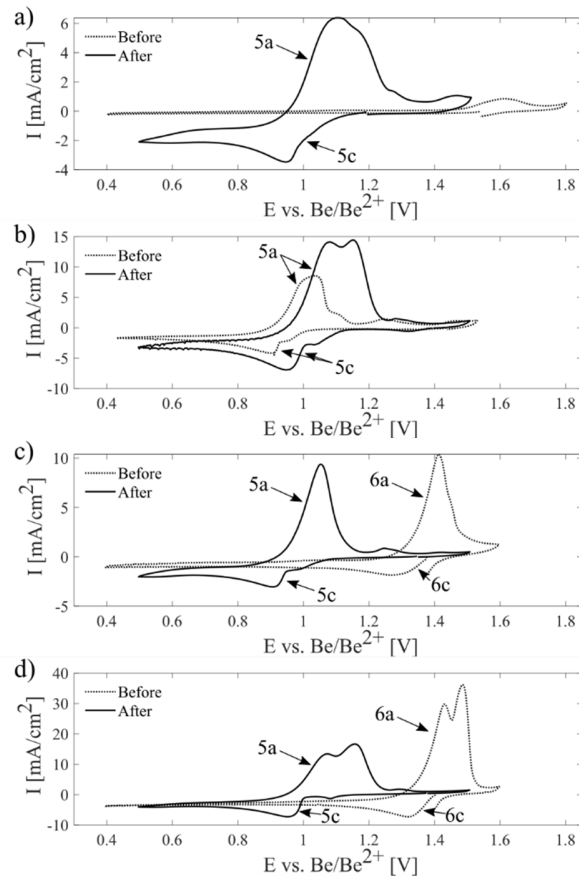


Figure 1. Cyclic voltammograms of corrosion FLiBe salts before and after 1000 hour exposure in a) capsule 1, b) capsule 2, c) capsule 3 and d) capsule 4. Scan Rate 80 mV/sec, Mo WE, Be/BeF₂ dynamic reference electrode, Glassy Carbon CE.

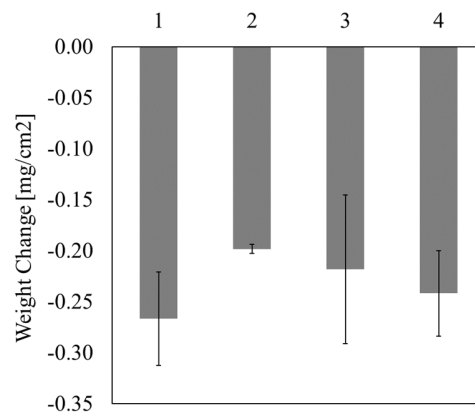


Figure 2. Weight change of 316H following exposure to salts in capsules 1 through 4 for 1000 hours at 700 °C.

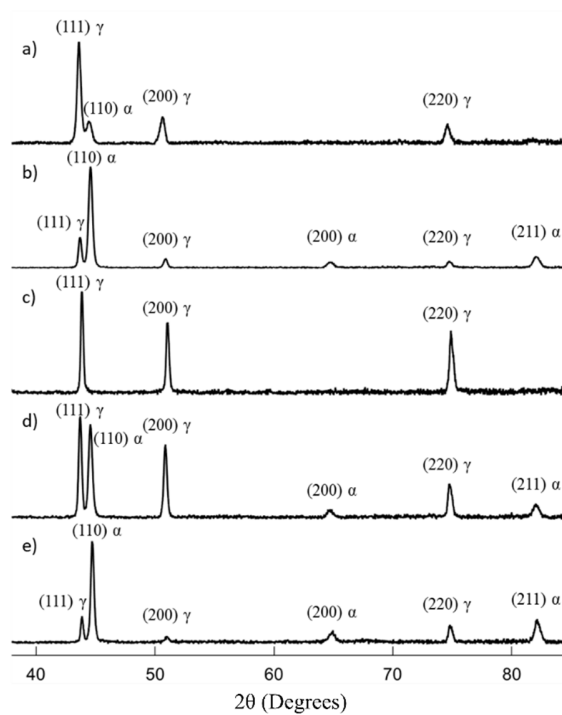


Figure 3. XRD patterns of 316H exposed to (a) as-received 316H, (b) as-purified FLiBe, FLiBe with (c) 245 ppm CrF_2 , (d) 99 ppm FeF_2 and (e) 392 ppm FeF_2 after 1000 hours at 700 °C.

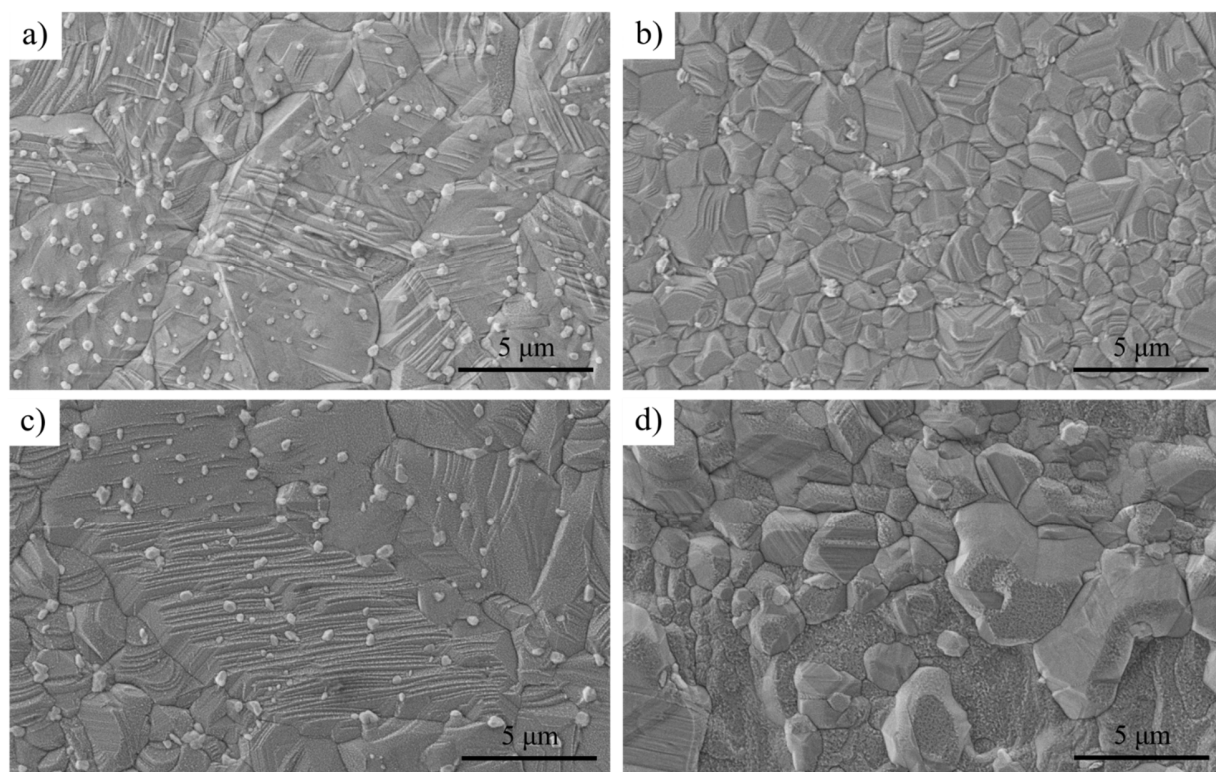


Figure 4. SEM image of corroded 316H surface exposed to (a) as-purified FLiBe, FLiBe with (b) 245 ppm CrF₂, (c) 99 ppm FeF₂ and (d) 392 ppm FeF₂ after 1000 hours at 700 °C.

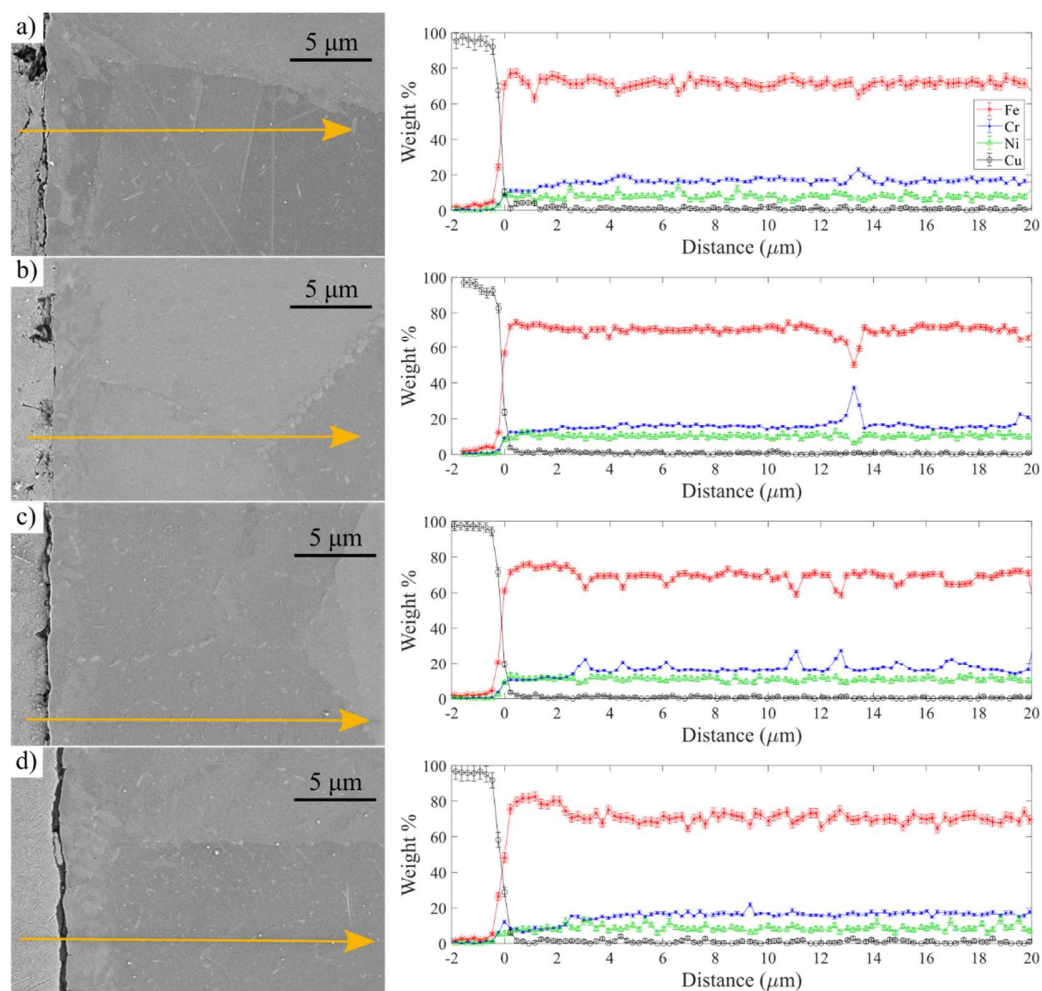


Figure 5. EDS line scan of near-surface region of 316H exposed to (a) as-purified FLiBe, FLiBe with (b) 245 ppm CrF_2 , (c) 99 ppm FeF_2 and (d) 392 ppm FeF_2 after 1000 hours at 700 °C.

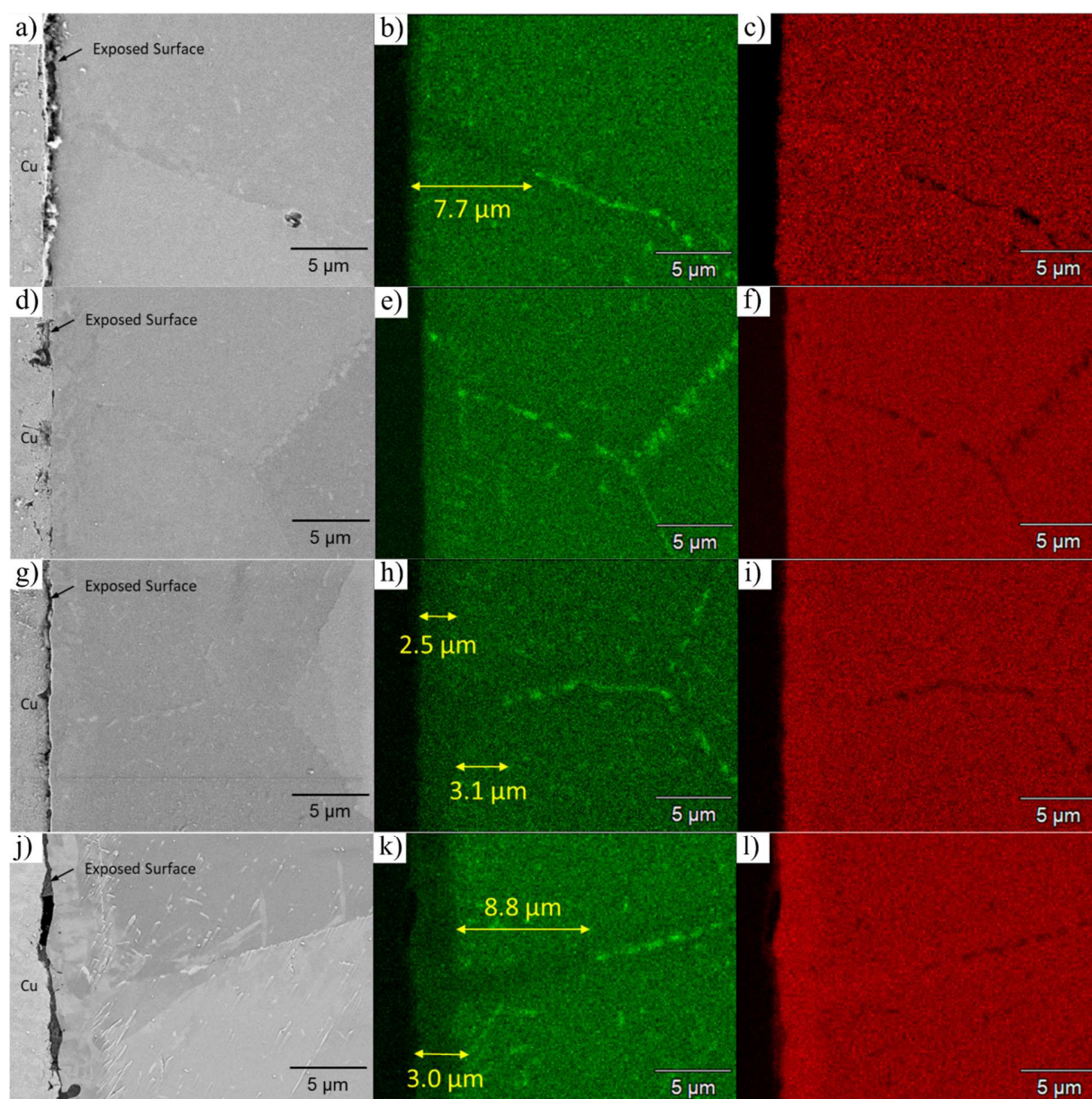


Figure 6. SEM & EDS line scan of near-surface region of 316H exposed to (a)-(c) as-purified FLiBe, FLiBe with (d)-(f) 245 ppm CrF_2 , (g)-(i) 99 ppm FeF_2 and (j)-(l) 392 ppm FeF_2 after 1000 hours at 700 °C. (a), (d), (g), (j) SEM image, (b), (e), (h), (k) EDS chromium map, (c), (f), (i), (l) EDS iron map.